ATMOSPHERIC RESEARCH

Theoretical design and preliminary tests of two new particle spectrometers for cloud microphysics research

R.P. Lawson, R.H. Cormack

SPEC, Incorporated, Boulder, CO 80301, USA

Theoretical design and preliminary tests of two new particle spectrometers for cloud microphysics research

R.P. Lawson, R.H. Cormack

SPEC, Incorporated, Boulder, CO 80301, USA

Abstract

Reliable cloud microphysical measurements can lead to a better understanding of the development of precipitation and cloud radiation. However, imaging of cloud particles with sizes $< \sim 200\ \mu m$ has been limited to small (collected) samples of high-quality photographs or large quantities of poor-quality digital images. Here we introduce two new instruments with demonstrated abilities for improved measurements of cloud drop spectra, liquid water content and digital imaging of the size and shape of small ice crystals. The first instrument uses digital holography to increase the sample volume over that possible with in-focus imaging of small particles. The digital holograms can be processed automatically and are expected to reveal the size and shape of small ice crystals, and the three-dimensional concentration, spacing and liquid water content of cloud drops. The second instrument measures cloud drop spectra and liquid water content from high-resolution measurements of forward-scattered light from an ensemble of drops. This eliminates inherent problems of coincidence and the small sample volume associated with single-drop measurements of drops. The theory of measurement and results from tests of both instruments are presented.

1. Introduction

The 1970's saw the introduction of the Particle Measuring Systems (PMS) airborne optical spectrometers for atmospheric research (cf., Knollenberg, 1981). Particle spectrometers employing optical scattering and imaging techniques have been installed on many research aircraft and analysis of collected data has done much to increase our understanding of cloud microphysics. However, careful analysis of the data shows that improvements in the measurements are still needed

to explain certain critical microphysical processes in clouds. Some examples follow:

Development of the drop spectra in cumulus clouds plays an important role in the formation of precipitation via the warm-rain (coalescence) process (Beard and Ochs, 1993). Yet, measurements of drop spectra are still limited to fairly good estimates from tedious analysis of samples, such as collected on soot-coated slides (Baumgardner, 1983), or high-rate measurements from optical probes such as the PMS Forward Scattering Spectrometer Probe (FSSP), which is subject to some significant measurement uncertainties (Baumgardner et al., 1985; Cooper, 1988; Brenguier, 1989). A promising alternative to the FSSP for sizing cloud drops is the new Aerometrics Phase Doppler Particle Analyzer (PDPA). The PDPA has been shown to reliably size drops in sprays (Bachalo and Houser, 1984; Oldenberg and Ide, 1990), however, an airborne version has yet to be flown. Both the FSSP and PDPA use single-particle measurement techniques. Therefore, they are limited to very small sample volumes which restrict their ability to measure the "tail" of the drop spectra, the region which is most influential in coalescence. The Malvern particle sizer (Swithenbank et al., 1977; Hirleman et al., 1984) does not suffer from the problems associated with single-particle measurement, but it has only been used in ground-based measurements of industrial sprays. Also, the data processing software is proprietary, which is not attractive for research applications.

Entrainment and mixing has a measurable effect on cloud liquid water content (LWC), the lifetime of cumulus clouds and the development of precipitation (cf., Cooper and Lawson, 1984). Blyth (1993) argues that entrainment and mixing influences the development of cloud particles and precipitation in a major way. One method of investigating the entrainment and mixing process is the effect it has on the evolution of drop spectra (Baker et al., 1984) and another is the spacing between the drops themselves (Baker, 1992). However, limitations of the FSSP (the current instrument of choice for these studies) makes it difficult to interpret the measurements and understand the physics of the process.

Hot-wire instruments currently used to measure LWC are also subject to significant measurement limitations (e.g., Strapp and Schemenauer, 1982; Biter et al., 1987). Newer optical techniques have been developed (e.g., Blyth et al., 1984; Gerber, 1992), however, these instruments have yet to be rigorously evaluated in an airborne environment. Reliable measurements of LWC are needed for studies of the development of precipitation, aircraft icing, cloud chemistry and cloud radiation.

The cold rain precipitation process is initiated by the formation of ice in clouds (cf., Pruppacher and Klett, 1978). The cold-rain process is thought to be responsible for much of the precipitation over continental regions outside of the tropics, for example, the high plains in the western United States (Dye et al., 1974). However, the detection and identification of ice crystals with sizes $< \sim 200 \, \mu m$ is not possible with optical imaging instruments currently used for that purpose, such as the PMS optical array probes (Heymsfield and Baumgardner, 1985).

Also, while collection and analysis of small ice crystals on slides provides good

photographic detail of the crystals themselves (Cooper and Vali, 1981), the analysis process is tedious and the spatial resolution in cloud is poor. Since the cold-rain process may often start with the formation of small ice crystals, a measurement of the size, shape and location of these particles could lead to a better understanding of the physics associated with cold rain. Quantification of the size and shape of small ice particles will also lead to better estimates of the radiative effects of cirrus clouds (Dowling and Radke, 1990; Heymsfield et al., 1990; Wielicki et al., 1990).

Thus, the current technology for measuring small (<200 μm) cloud particles is limited to fairly good measurements with coarse spatial resolution (using collection techniques), or high-rate measurements which contain significant uncertainties (using optical techniques).

Here we introduce two new optical instruments that are designed to provide improved measurements of cloud drops and ice crystals. The first of these is a Digital Holographic Imaging System (DHIS) which is capable of making shadowgraphs with very fine (order few μm) size resolution of ice particles and cloud drops. The DHIS can also measure the size and three-dimensional spacing of cloud drops (and thus the LWC). The second instrument measures the forward-scattered light from an ensemble of cloud drops. The measurements of scattered light intensity are made with an angular resolution of 0.035° and (independent) computations of LWC and drop spectra are made in software.

2. Digital Holographic Imaging System (DHIS)

2.1. Depth of field

Shadow images of cloud particles can be generated by casting laser light on an object and recording the image using an array of photodiodes. Knollenberg (1970) measured the depth of field (DOF) for oblique spheres using an isodensitometer in the laboratory and found

$$DOF \approx \frac{6r^2}{\lambda},$$ (1)

where r is particle radius, λ is the wavelength of coherent light, and here, DOF is the in-focus image.[1] The DOF and therefore the sample path decrease with the square of particle size. For example, using Eq. (1) with $\lambda=0.78$ for particles with $d=2r=5$ μm, the $DOF \approx 50$ μm and for $d=50$ μm the $DOF \approx 5$ mm. Thus, limiting the sample path of an airborne cloud particle spectrometer to the optical DOF generally results in a very small sample volume, while alternatively, accepting particles outside the DOF, results in large uncertainties in the sizing and concen-

[1] Korolev et al. (1991) put Knollenberg's work on a more sound theoretical basis and expanded the measurements.

tration of smaller particles (cf., Heymsfield and Baumgardner, 1985; Korolev et al., 1991).

An attractive alternative to in-focus imaging of cloud particles is the use of in-line holography. In-line holography was originally developed by Gabor (1949) to improve the resolution of electron microscopy. The process uses a single coherent (laser) light source and numerically recovers the images from the (predictable) interaction of the undeviated laser beam and light scattered from the particles. The images are actually diffraction patterns, so that the holographic *DOF* can be much larger than that for in-focus imaging. Cormack and Lawson (1993a) show that the *DOF* for a Gabor holographic imaging system using a pulsed laser can be expressed as

$$DOF = L_{coh} \frac{\sqrt{1-NA^2}}{1-\sqrt{1-NA^2}}, \qquad (2)$$

where $NA = \sin(\theta_{max})$ is the numerical aperture of the system, θ_{max} is the largest angle from the optical axis that a ray can have and still traverse the optical system, and L_{coh} is the coherence length of the laser. For the small apertures required by a solid-state television camera ($\theta \leqslant 4°$, $NA \leq 0.07$), we can approximate Eq. (2) by

$$DOF \approx \frac{2L_{coh}}{NA^2} \geqslant 400\, L_{coh}. \qquad (3)$$

For the high-power ($2 \rightarrow 50$ W) laser diodes used in the DHIS, $L_{coh} \approx 0.5$ mm resulting in $DOF = 200$ mm. Thus, from Eq. (1) and Eq. (3) it can be seen that compared with a conventional imaging system, the DHIS extends the *DOF* for particles with diameters $< 30\ \mu$m by three orders of magnitude. Because the *DOF* is usually the limiting factor in defining the sample volume of an airborne imaging instrument, the DHIS can achieve a substantial increase in sample volume for imaging small cloud particles.

2.2. Description of instrumentation

The DHIS uses digital techniques to record in-line holograms and reconstruct images. The DHIS optical system is shown schematically in Fig. 1. Light from the pulsed laser diode is spatially filtered by focusing the beam through a 100 μm pinhole before collimation, thereby improving the laser output by removing some of the multi-mode structure, producing a more uniform beam. The light then passes through the sample volume before being condensed onto a Charge Injection Device (CID) camera (Cidtek CID2250) with a 512×512 array of photodiodes. The camera lens system consists of two lenses spaced by the sum of their focal lengths, with a *NA*-limiting aperture at the common focal plane. This telecentric configuration has the property that the size of the image does not change with object distance. This eliminates the need for scaling the images, a time-consuming operation that often results in loss of information. The magnification of
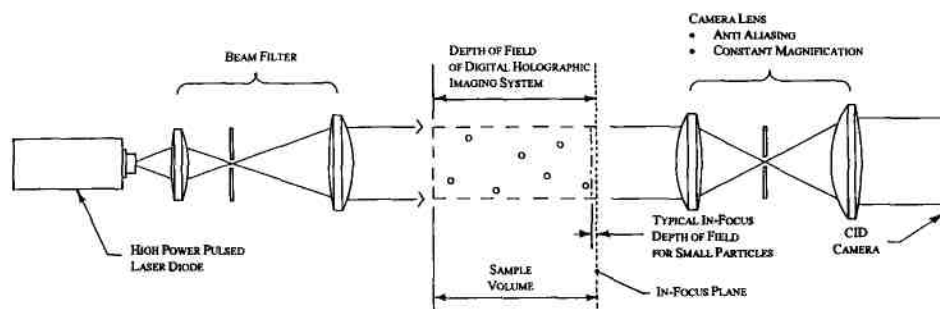
Fig. 1. Schematic drawing showing optics in Digital Holographic Imaging System (DHIS) and comparison of holographic depth-of-field with typical depth-of-field for conventional (in-focus) imaging system.

the lens system is numerically equal to the ratio of the focal lengths of the input and output lenses.

The sample volume for a DHIS with a 512×512 array is $(512\,x)^2\,DOF$, where x is the desired particle size resolution. The entire CID array can be read at a frame rate of 30 s^{-1} using a commercial frame grabber and video cassette recorder (VCR); however, custom 512×512 cameras and recorders with frame rates up to 240 s^{-1} are obtainable. A constant frame rate is used for studying fields of cloud drops where the concentrations of particles are relatively high (say, > 10 cm^{-3}) so that periodic recording always includes frames with cloud drops. Alternatively, a portion of a CID array can be read and the entire array reset in preparation for the next image, and this cannot be done with a charge-coupled-device (CCD) array. This latter technique can be used to reduce dead time during readout and effectively increase the sample volume for sparse populations of small ice crystals. In the DHIS, this is accomplished by a particle detection system positioned upstream of the holographic imaging system. This feature is especially useful in measuring low concentrations of small ice crystals, such as found in cirrus and newly-developing cumulus clouds. With the particle detection system, the DHIS is capable of acquiring particles with a mean size of 200 μm at a rate of about 100 s^{-1}. For real-time applications, a PC-486 computer is interfaced through a digital camera input board and contains a co-processor board. This type of system can reconstruct images from holograms and display them in real time.

2.3. Reconstruction of holograms

Cormack and Lawson (1993a) develop equations that describe both optical (i.e., film) and digital holographic systems. They then numerically simulate the systems and compare the results. When a hologram is recorded digitally, image reconstruction techniques are not limited to simulating optical reconstruction methods. The overall result is that the background variations in the digital hologram are removed, the object wave is distortion-free, and the (already small)

diffraction pattern overlay is reduced by division with the (larger) background (Cormack and Lawson, 1993a).

Fig. 2 shows a laboratory test set-up of the DHIS. The optics shown schematically in Fig. 1 were implemented with Spindler & Hoyer microbench components on an optical rail. (For tests in a wet wind tunnel, the microbench components were also placed in an airfoil strut similar to the installation of the Cloud Drop Spectrometer shown in Fig. 12.) To test the recovery of images from holograms at the limiting resolution of the optical system, images and holograms were made of a 5 μm diameter wire. The image of the wire is precisely one pixel wide on the CID camera, and represents the designed limit of resolution of the optical system. Fig. 3a shows the in-focus image of the wire. Fig. 3b is the hologram of the wire at a distance of 5 mm, Fig. 3c is the image digitally re-constructed from Fig. 3b and Fig. 3d is the inverse of Fig. 3c. The full resolution of the in-focus image is recovered in the image re-constructed from the hologram, and there is no observable ghosting or other artifacts due to aliased detection of the hologram. The resolving power of the digital holographic system is ultimately a function of the optics and wavelength of the light source; a size resolution of ~ 2 μm is achievable with common laser diode sources.

Fig. 4 shows an in-line hologram of a water suspension of 30 μm polystyrene spheres in a spectroscopic test cell. The ring patterns are caused by the interference between the Fresnel diffraction patterns of the spheres and the un-diffracted
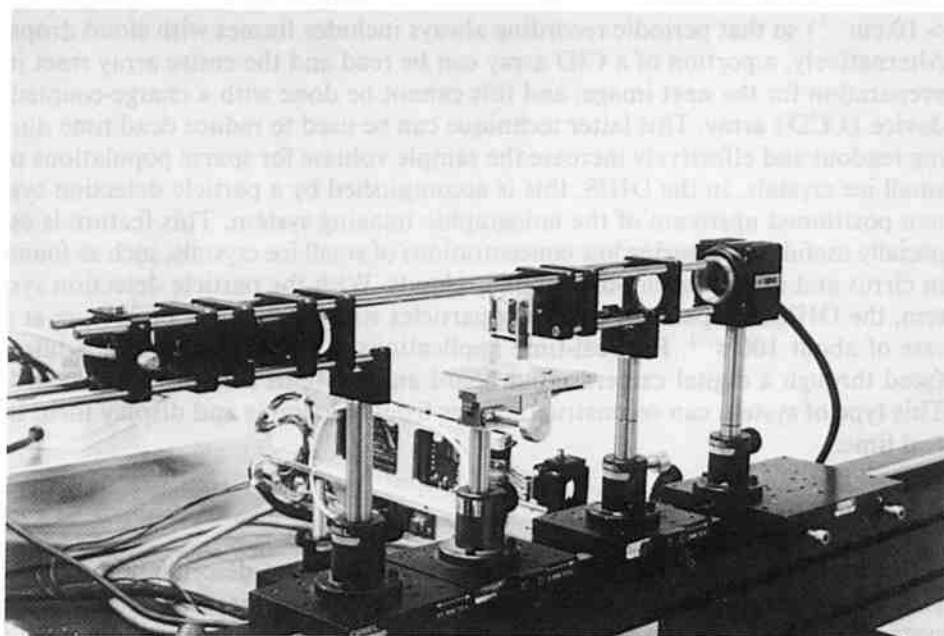

Fig. 2. Photograph showing Spindler–Hoyer microbench optical components system used to construct DHIS in the laboratory. Pulsed laser diode is at left side of optical rail, sample volume is in the middle and CID camera is at the right side of rail.
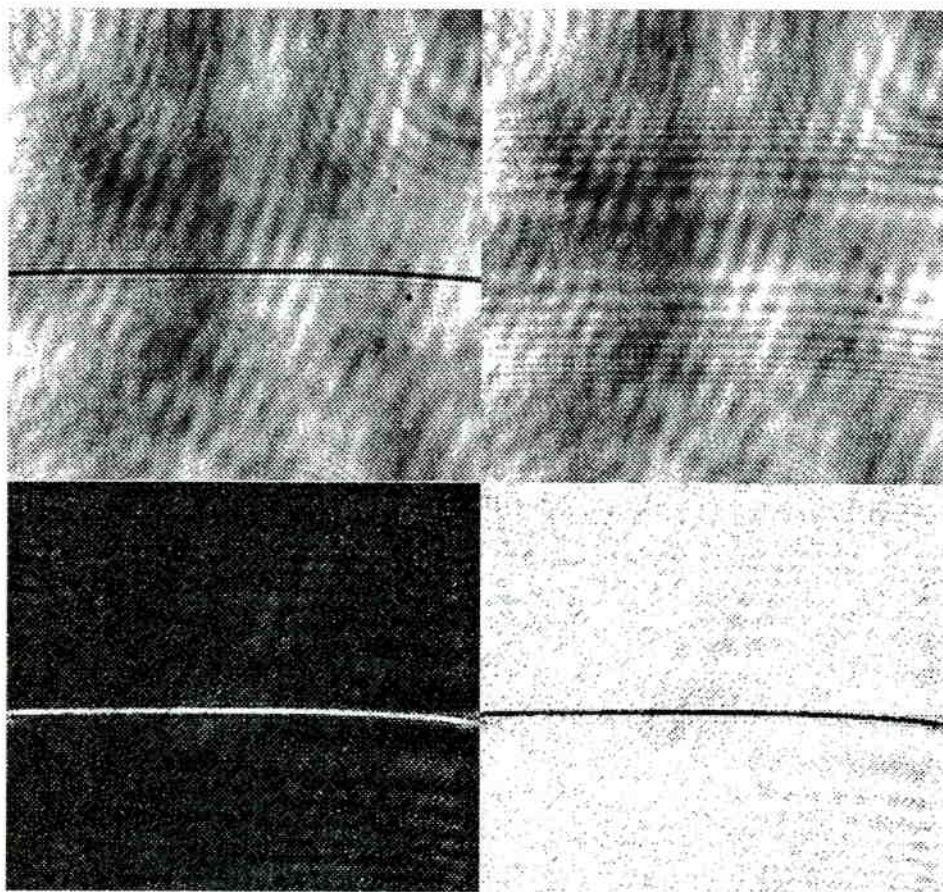
Fig. 3. In-focus image of a 5 μm wire (upper left); Hologram of wire at 1 cm out-of-focus (upper right). The bottom images are images digitally reconstructed from the hologram.

background beam. The upper image in Fig. 5 shows a section of the hologram shown in Fig. 4 taken from the near the upper right corner. The lower two images in Fig. 5 show two different techniques of extracting the images from the hologram digitally. The left image (labeled "Optical" Process) is a digital simulation of the process of optically re-creating an image from a hologram. Essentially, the Huygen–Fresnel equation (Born and Wolf, 1965) was applied directly to the stored hologram image. This image compares well with actual images from similar holograms recorded on film and reconstructed optically (e.g., Grabowski , 1983). The right image (labeled "Digital" Process) shows the very large increase in Signal/Noise (S/N) that can be achieved by using the modified digital hologram. Fig. 6 shows surface plots of the lower images in Fig. 5 . The point-of-view of these plots is looking down from above the top left corners of the lower images in Fig. 5. The surface plots show dramatically how much the S/N is improved by digital processing. Fig. 7 shows a three-dimensional re-construction of the size
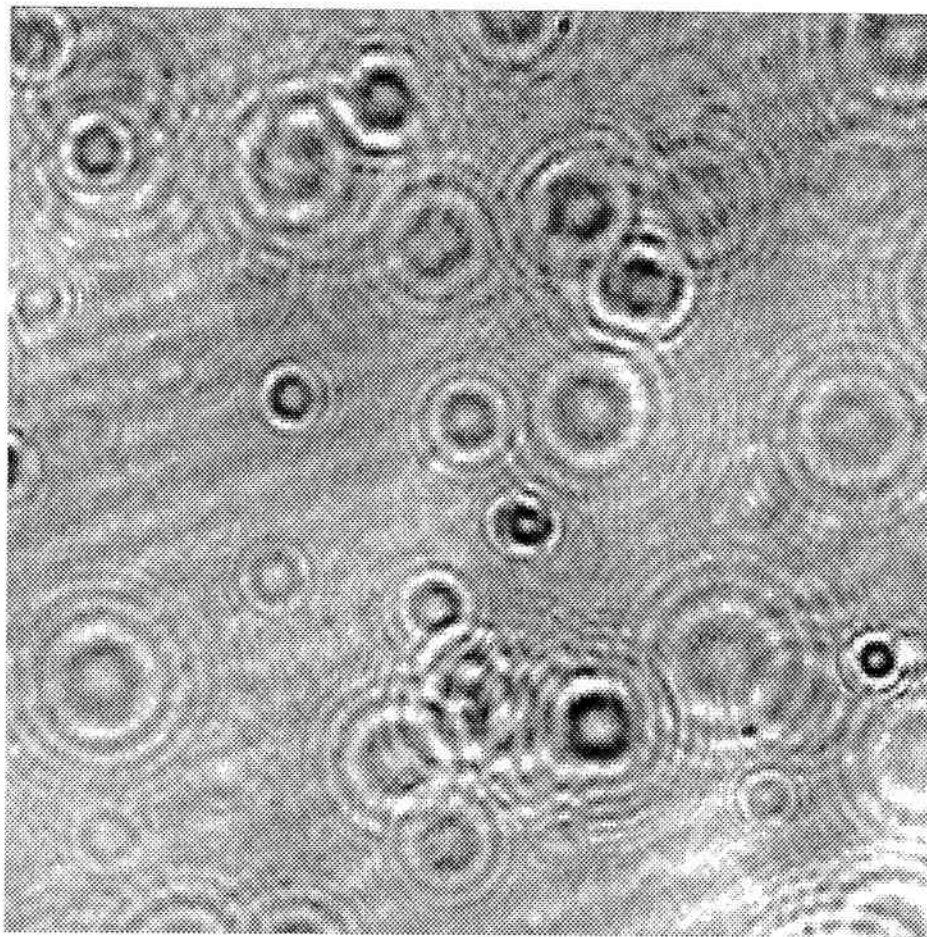
Fig. 4. Hologram of 30 μm polystyrene spheres in aqueous solution produced in the laboratory using the Digital Holographic Imaging System (DHIS).

and spacing of the polystyrene spheres from the hologram shown in Fig. 4.

The improved S/N seen in Fig. 6 enables for the first time *reliable* automated processing of the size and location of cloud drops in a hologram. This is an important consideration because manual processing of 1 l of data often requires days or even weeks (cf., Kozikowska et al., 1984; Trolinger, 1985; Brown, 1989). Previous attempts to automatically process optical holograms (e.g., Bexon et al., 1976; Zarschitzky, 1985) have often yielded unreliable results because of the in-

---

[2] A recent processing advancement using digital TV to capture and view optical holograms was achieved by Borrmann and Jaenicke (1993). They found that this reduced analysis time slightly and the minimum detectable droplet diameter from about 12 μm (Brown, 1989) to about 6 μm. However, the S/N was still inadequate to automatically identify the particles and drops with diameters < 10 μm required increased post-processing magnification and special human attention.
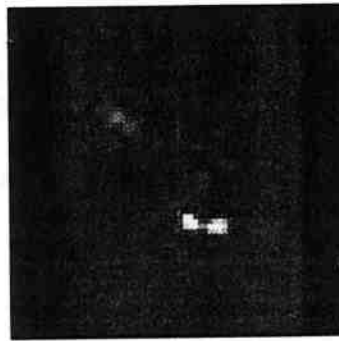
Hologram
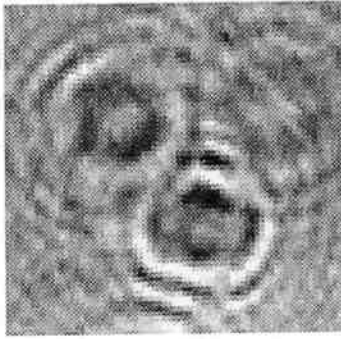
Image   Image
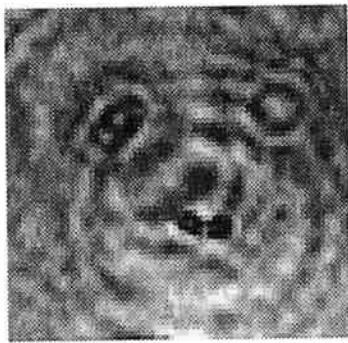
("Optical" Process)   ("Digital" Process)

Fig. 5. Portion (top) extracted from upper right part of hologram shown in Fig. 4 and comparison of images reconstructed using (lower left) optical and (lower right) digital processes (image recovered using digital process shown in reverse video).

herent low S/N (Borrmann and Jaenicke, 1993).[2] An example of a hologram and a three-dimensional reconstruction of water drops in motion captured by the DHIS in a small wind tunnel is shown in Fig. 8. An automated three-dimensional numerical reconstruction of the size and location of the drops is possible because of the strong S/N seen in the surface plots and reconstructed images of the drops, as shown in Fig. 9. The height and consistency of the S/N seen in Fig. 9 strongly suggests that reliable automated processing of DHIS holograms of cloud drops is obtainable. The accurate drop sizing and concentration obtainable from measurements such as shown in Fig. 8 can provide excellent "what-you-see-is-what-you-get" (WYSIWYG) measurements. With a 5 μm (pixel) resolution, the DHIS is capable of about 2 μm drop-size resolution. This sub-grid resolution is possible because the light intensity received on each pixel is digitized to one part in 256

and the level of charge in the pixels that are not saturated (in the reconstructed in-focus image) can be analyzed to estimate the sub-grid contribution to drop size. The snapshot WYSIWYG measurements should provide valuable baseline calibrations of continuous measurements of LWC and drop spectra from other instruments. In addition, automated analysis of fields of cloud drops (such as shown in Fig. 8) may facilitate investigations of the mixing process using three-dimensional analyses similar to the one-dimensional fishing statistic developed by Baker (1992).

Another application of the DHIS is to provide automated (shadowgraph) images of the fine details of small ice crystals. An example of the capability of the DHIS to capture and reproduce the fine structure of small particles is seen in Fig. 10, which shows one barb of a small Guinea feather. The optical system used in the DHIS for these images was re-configured to have a maximum resolution of 3 μm. Shown at the top in Fig. 10 is an in-focus image of the barb, in the middle is a hologram and at the bottom is an image numerically reconstructed from the hologram. The small barbules seen in both images range from 5 to 15 μm in width. In the hologram, information about the fine details is contained in the small interference fringes seen throughout the image. The quality of the image numerically reconstructed and shown in the right image in Fig. 10 is excellent and demonstrates the ability of the DHIS to reproduce the shapes of small ice crystals.

"Optical" Image Reconstruction
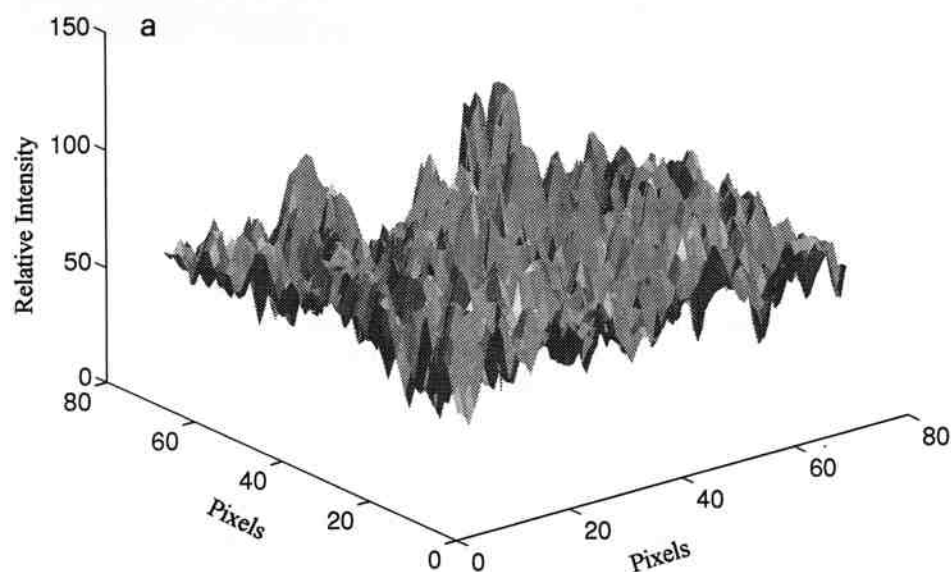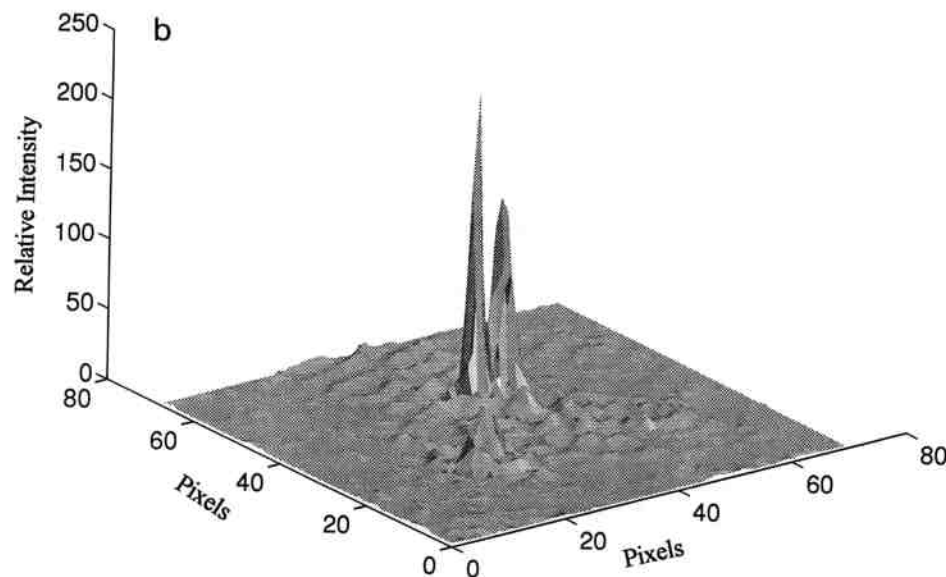
"Digital" Image Reconstruction

Fig. 6. Surface plot of (left) reconstructed image using optical process shown in Fig. 5 at lower left, and (right) surface plot of reconstructed image using DHIS process shown in Fig. 5 at lower right. Horizontal axes are in units of (5 μm) pixels and vertical axis is relative intensity. Comparison demonstrates significantly increased signal-to-noise of DHIS process.

This aspect of the instrument will be particularly useful in studies of ice crystals in visible and subvisible cirrus, and in studies of the origin of ice crystals in water clouds.

3. Cloud drop spectrometer

3.1. Description of instrumentation

Measurements of the size spectra of cloud droplets were improved by the introduction of the FSSP (Knollenberg, 1981). However, inherent limitations of the FSSP result from the single-drop measurement scheme; i.e., measurement of the forward scattered light from a single particle results in a small sample volume and introduces coincidence errors (Baumgardner et al., 1985; Brenguier, 1989).

The Cloud Drop Spectrometer (CDS) measures forward scattered light from an ensemble of drops in a relatively large (order 10 cm^3) sample volume. As

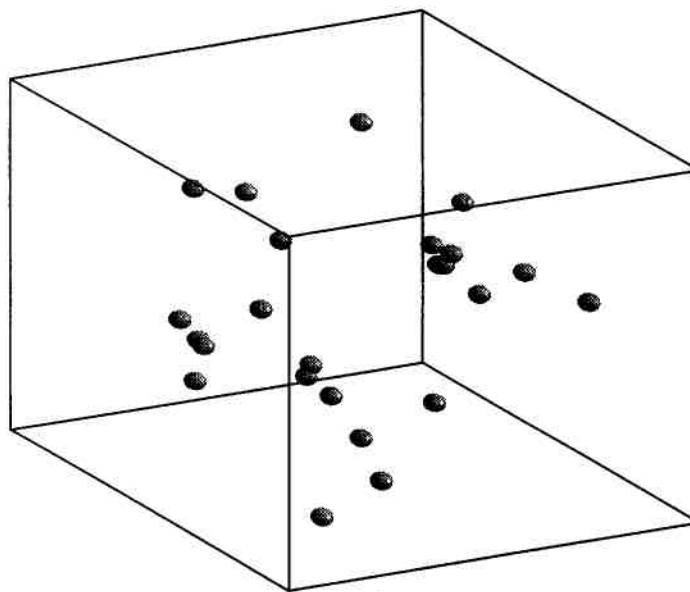Fig. 7. Three-dimensional reconstruction showing positions of 30 μm polystyrene spheres from holo-gram in Fig. 4. Size of cube is approximately 1 mm high by 1 mm deep by 5 mm across (spheres shown larger than actual size for sake of clarity).

shown in the schematic drawing of the CDS in Fig. 11, forward scattered light is measured with high angular resolution using a linear array of 256 CCD photode-tectors. The electro-optical components were packaged in Spindler–Hoyer micro-bench miniature rails and optics holders. The microbench components are very sturdy and precise, yet the component arrangement is flexible and can be readily modified. The components were mounted on an optical bench in the laboratory and later packaged in an airfoil strut for tests in an icing wind tunnel (see pho-tographs in Fig. 12).

Since airborne instruments that depend on precise optical alignment are gen-erally not robust, the CDS was designed so that alignment changes do not have overriding effects on the data. Instead of weighting and summing *in hardware* the individual components of the scattered light, we have eliminated the variable density filters and single photodetectors used in other devices (e.g., Blyth et al., 1984; Gerber, 1992) and replaced them with a multi-element photodetector ar-ray. Fig. 13 shows schematically the 256-photodiode CCD array (EG&G model RL0256 TBQ) and an example of a diffraction pattern of light scattered from a single drop. The photodiode array has high aspect-ratio pixels with dimensions of 50×2500 μm and measures the scattered light at about 240 discrete angles.

The precision V-shaped mask shown in Fig. 13 is made from a photographic process using graphics art film. The mask increases the dynamic range by occult-ing the active area of the CCD array at the smaller angles where the scattered light intensity is much greater than at the larger angles. Since the angular intensity of

the scattered light is inversely proportional to drop radius, it is important to be able to measure light at very small angles (say, $<0.1°$). The unscattered beam focuses to a spot with an intensity 10^6 times that of the scattered light only $100 \rightarrow 200 \ \mu m$ away, where measurement must begin. The mask material must completely absorb the focused light (0.1% scatter significantly corrupts the measurements) while remaining nearly transparent a few μm away. With careful exposure control, thick emulsion, high contrast, graphics art film (Kodak Ektografic HC) is capable of this kind of performance. The film density can be adjusted so that just enough of the focused beam penetrates for position and relative intensity measurements by the CCD array, while maintaining 75% transmission values and $<5 \ \mu m$ resolution over nearby pixels.

The mask cannot be placed directly onto the surface of the CCD array due to the glass cover plate bonded over the CCD chip. If the mask is placed on the cover plate, then there is an unavoidable 1 mm gap between the mask and the active photodiodes of the CCD array. Since some light scattering occurs within the acetate substrate of the graphics art film, this small distance to the CCD pixels is enough to allow for significant blurring of the light pattern, especially at the smaller angles, where the light intensity changes rapidly from pixel to pixel. This causes the low-angle noise in the signal to become partially signal-dependent, a situation nearly impossible to correct in software. To avoid this problem, an optical relay lens is used to relay the image of the mask directly onto the active surface of the CCD array. To further reduce the spurious scattered light, the laser diode is spatially filtered by passing the focused beam through a $100 \ \mu m$ pinhole before recollimating. This has the effects of reducing the intensity of the beam sidelobes, and hence the background scattered light seen by the CCD array. The cross section of the laser light is expanded to 6 by 18 mm and the sample path shortened to about 100 mm (i.e., $0.6 \times 1.8 \times 10$ cm).

The electronics in the instrument converts the distribution of scattered light on the CCD array to a video signal which is resolved over five decades of dynamic range. The signals from the CCD array are converted to video and then digitized by a 14-bit analog-to-digital converter. The signal processing electronics currently present digital data at a rate of up to 100 samples per second to an adapter board located in a PC-486 computer. Data rates up to about 1 kHz are possible. Data collected by the adapter board in a PC-486 computer are read, processed, displayed in real time and raw data are written to a file by a dedicated C-language device driver. Using Matlab software, additional software was developed to process and display the archived data.

3.2. Recovery of liquid water content

Theory

The intensity of forward scattered light is measured at various positions in the focal plane of a condensing lens. This gives the amount of light scattered in the sample volume as a function of scattering angle, irrespective of where in the sample volume the scattering takes place. The intensity of light scattered by a cloud

droplet is a sensitive function of both the scattering angle θ and the droplet radius r. The intensity distribution for a single drop, $K(\theta,r)$, can be calculated from Mie theory (Blyth et al., 1984).

A clever method of determining LWC from the scattered light measurements was introduced by Chittenden (1976) and discussed in Blyth et al. (1984). As shown in Fig. 13, the scattered light is sampled at a number of discrete angles, θ_j, $j=1 \rightarrow M$. An output function, $F(r_i)$, can be defined on discrete values of the radius, r_i, $i=1 \rightarrow N$, as the weighted sum of the light received at the discrete angles;

$$F(r_i) = \sum_{j=1}^{M} K(\theta_j,r_i) * W_j, \quad (i=1 \rightarrow N), \quad \text{or} \quad \vec{F} = K * \vec{W}, \tag{4}$$

where $K(\theta_j,r_i)$, the scattering function, is normalized to represent the light scattered by one unit volume of particles of radius r_i, and W_j is the weighting value
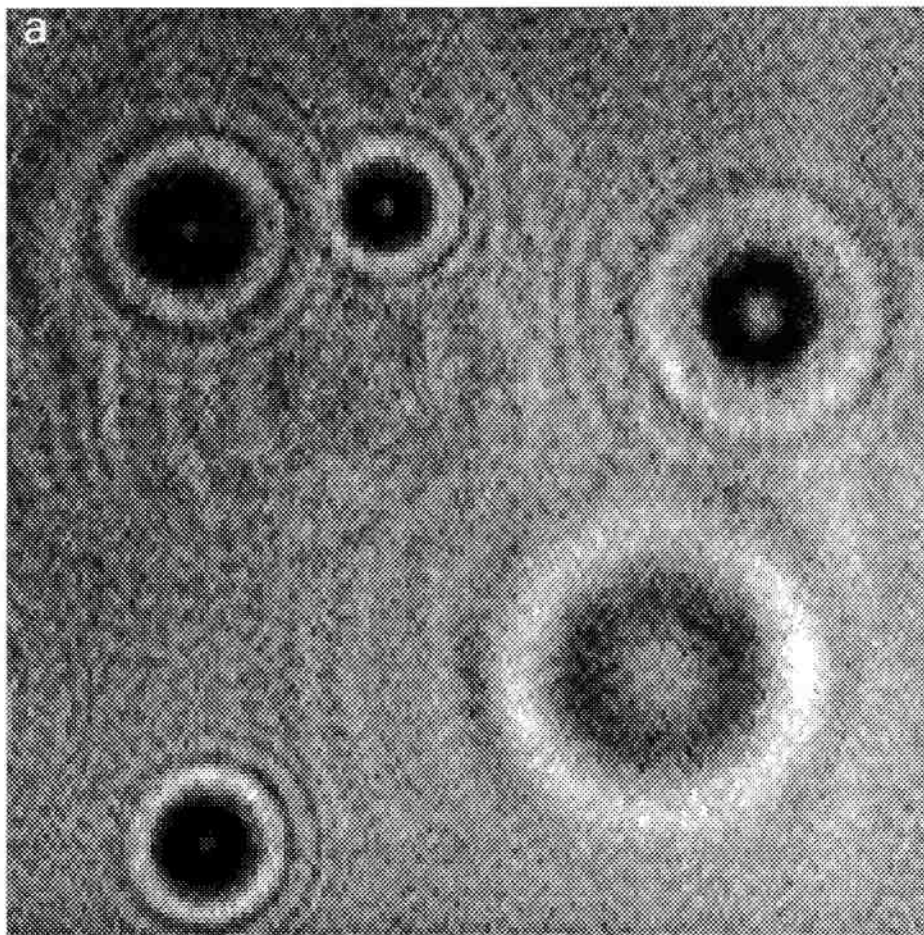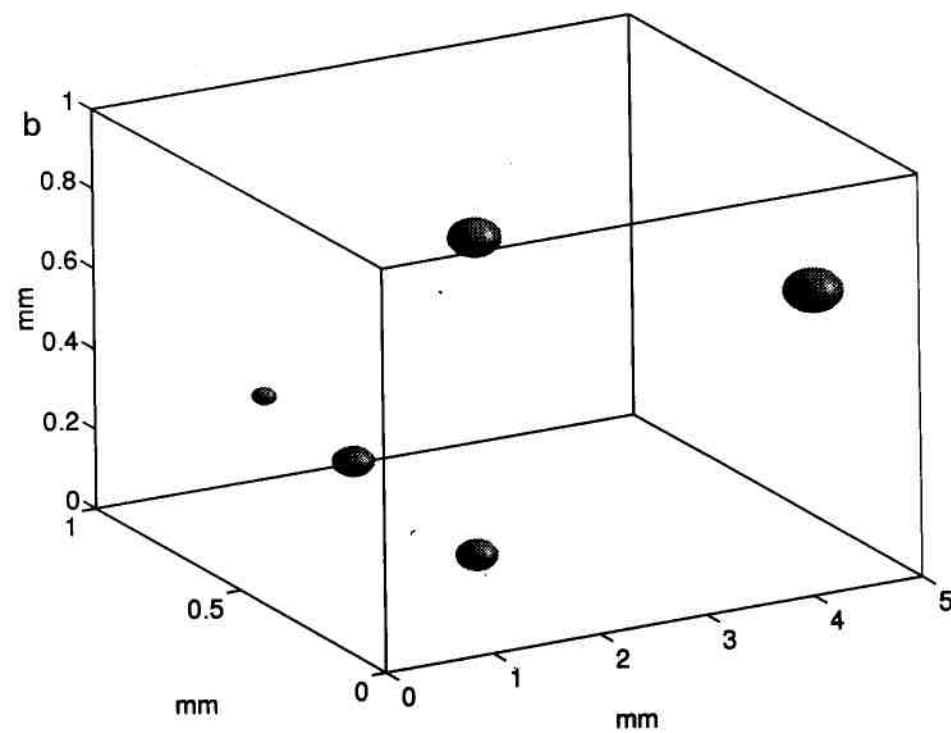
Fig. 8. Hologram (left) and (right) three-dimensional reconstruction showing positions of 1 5–40 μm diameter water drops captured in motion by the DHIS (spheres shown larger than actual size for sake of clarity).
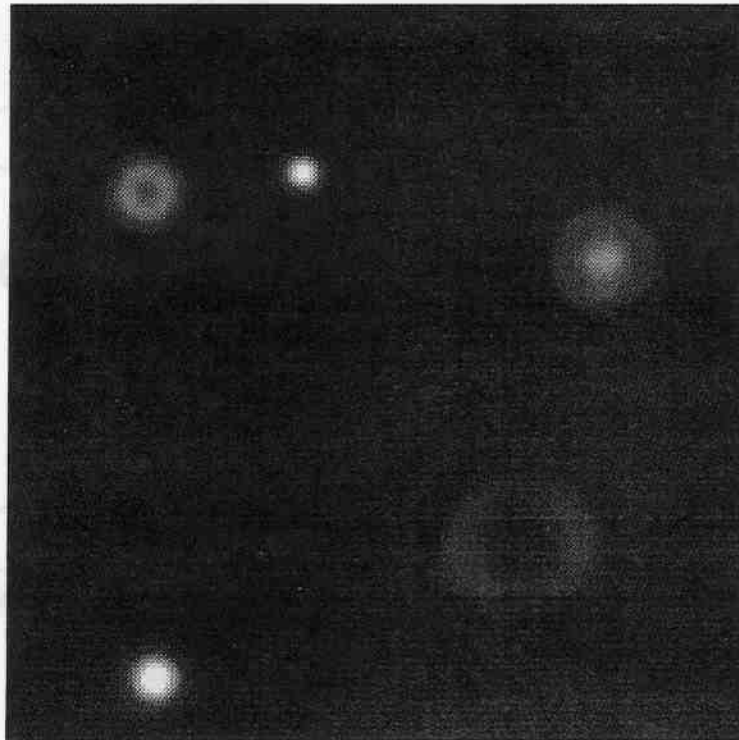
for angle θ_j (i.e., the weight for detector j). If weights W_j can be found such that the output function is proportional to the volume of the drops, i.e.; $F(r) \propto Cr^3$, then the output of the instrument will be proportional to LWC regardless of the specific size spectrum of the cloud drops in the sample volume.

To find the weights $\vec{W}$, an output function, $\vec{F}$, is defined and then Eq. (4) is inverted. The problem is to create the desired function from a sum of diffraction functions, i.e., the columns of K. These diffraction functions are not orthogonal to each other, hence completely arbitrary output functions cannot be formed. This problem is addressed by limiting the range (r_i) of the output function to those radii which produce a significant amount of scattered light within the chosen range of θ.

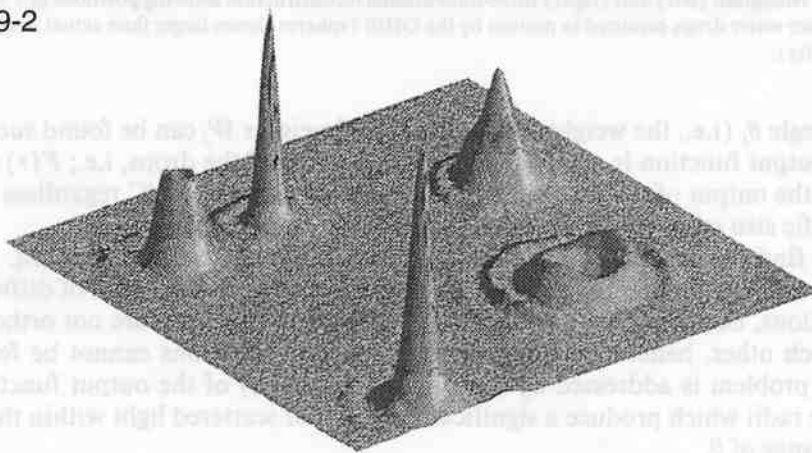The system of Eq. (4) can then be solved for the set of weights $\vec{W}$, that produce the output function with the minimum RMS difference from the target function. The weights must be non-negative only if they are implemented by optical filters, such as in the airborne device described by Gerber (1992), however, this constraint is not necessary here where the basis functions are weighted in software. Overdetermining the system (more r_i than θ_j) has been found to give a more
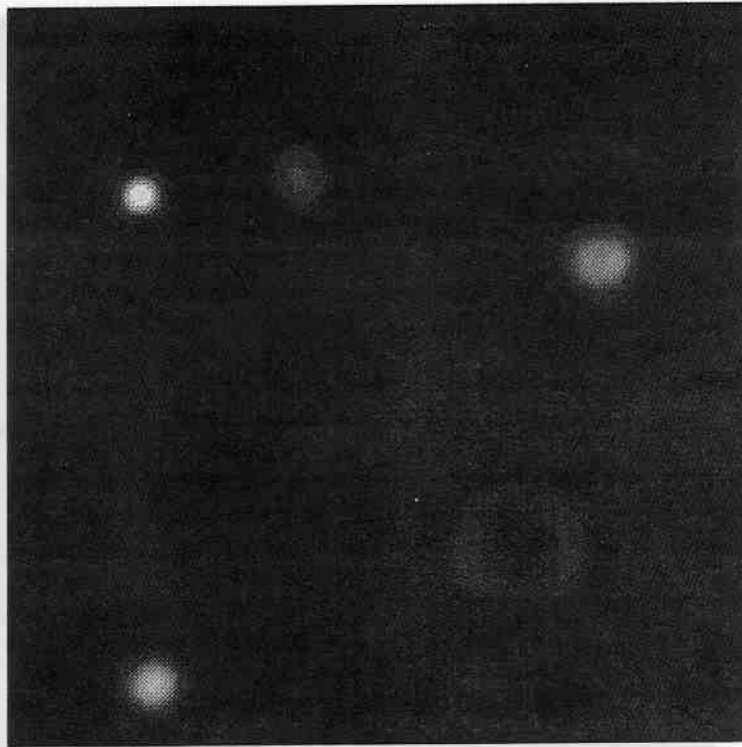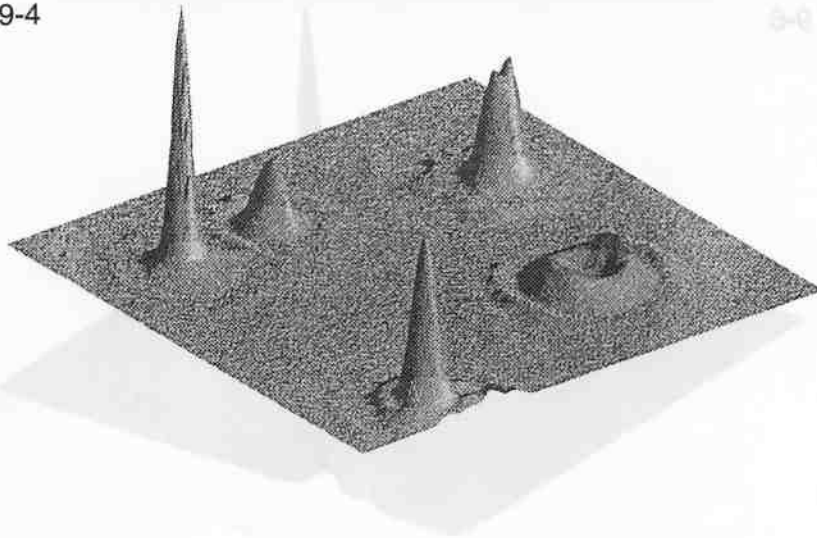
9-1

9-2

Fig. 9. Holograms (left) and (right) three-dimensional reconstruction showing positions of 1.5–40 μm diameter water drops measured in nature by the OAP. Features seem larger than actual size because of charts.

for angle θ_i (i.e., the weights ... for P_i^* can be found such that the output function ... given basis functions, i.e., $P_i^*(\kappa C)^*$, then the output ... regardless of the specific ...

To find ... Eq. (4) is investigated ... different diffraction functions, ... not orthogonal to each other, ... cannot be formed. This problem is addressed ... of the output function to those radii which produce a significant ... scattered light within the chosen range of θ.

The system of Eq. (4) can then be solved for the set of weights H_i^* that produce the output function with the minimum RMS difference from the target function. The weights must be non-negative only if they are implemented by optical filters, such as in the arbitrary device described by Gerber (1982); however, this constraint is not necessary here where the basis functions are weighted in software. Overdetermining the system (more i than η) has been found to give a more
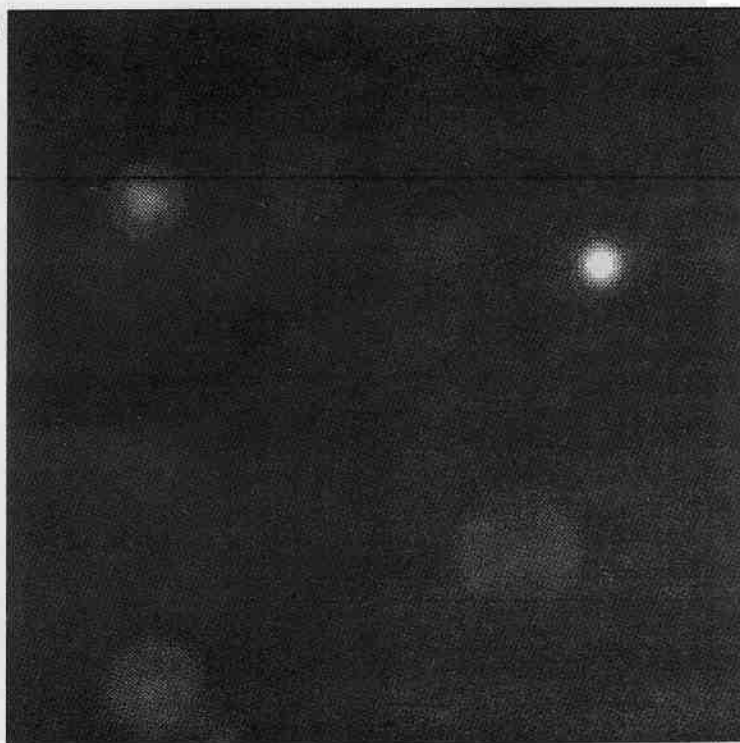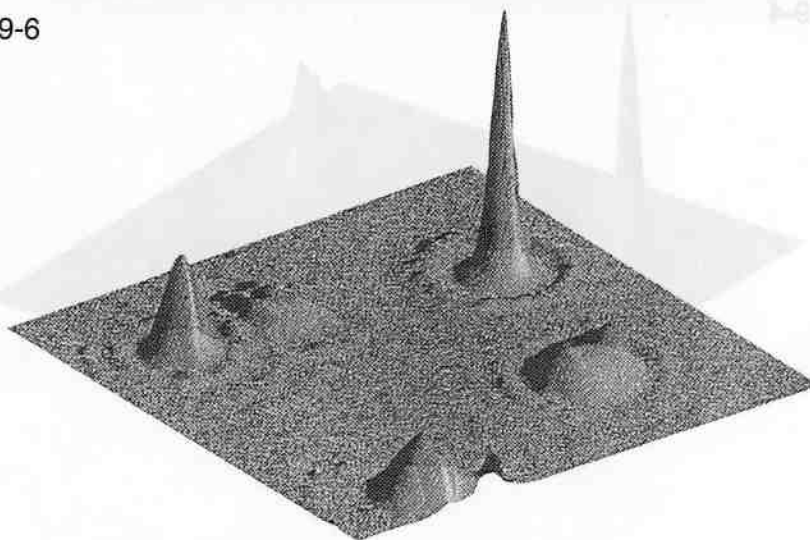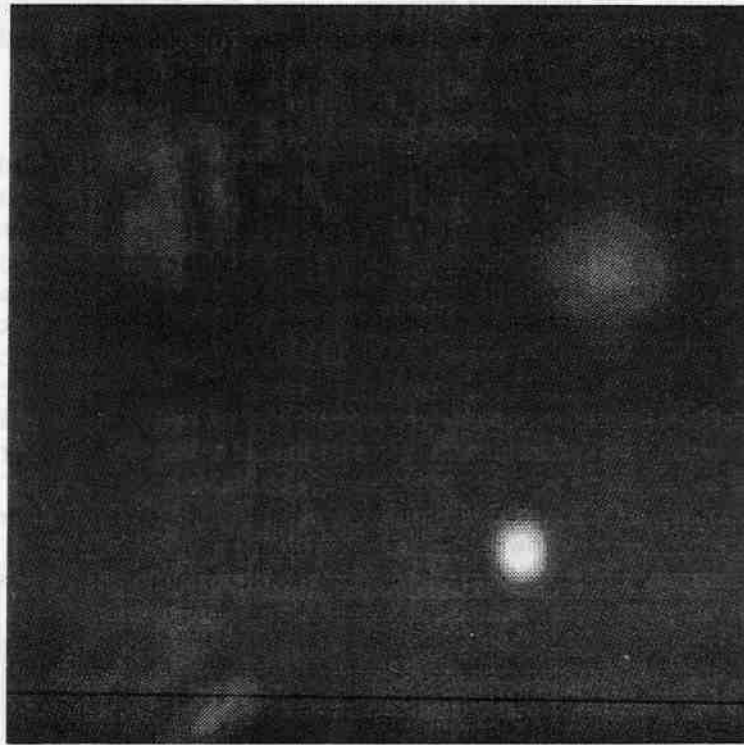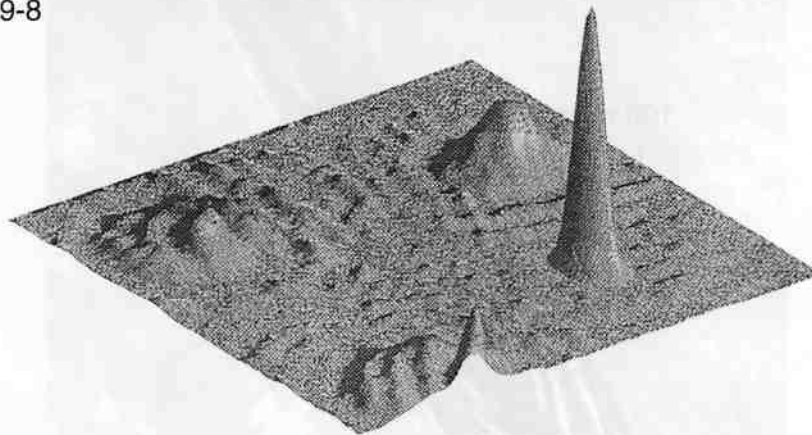
9-3

9-4

9-5

9-6

9-7

9-8

Fig. 9. Reconstructed images (upper) and corresponding (lower) surface plots from hologram of water drops shown in Fig. 8. Images were reconstructed from hologram by numerically stepping through sample volume. Corresponding surface plots show relative intensity of drops as focal plane is numerically stepped through sample volume and illustrate strong signal-to-noise ratio capable of supporting automated image processing.

stable solution. The technique provides a direct optical measurement of LWC that does not suffer from the uncertainties inherent to single-drop analysis, such as found with the FSSP.

Tests in an icing wind tunnel

A prototype of the CDS was built and tested in the icing wind tunnel operated by the National Research Council (NRC) of Canada in Ottawa, Ontario. The prototype CDS was constructed of Spindler–Hoyer Microbench components, which are very versatile and maintain rigid optical alignment (Fig. 12).

A problem that typically plagues in situ optical sensors is fogging and/or wetting of the optics in clouds. For example, Brenguier et al. (1993) discuss problems of icing and fogging of the optics in the FSSP. Based on numerical models of flow around aerodynamic bodies (Lawson and Rodi, 1992) and experience gained in the design of a SPEC precipitation imaging spectrometer (Lawson et al., 1993), custom non-wetting apertures (windows) were developed for the CDS. The wind tunnel was operated at 20°C at speeds from 10 to 95 m s^{-1} and the optics in the CDS showed *no* contamination, while at the same time the optics in the FSSP in the tunnel showed clear evidence of fogging (J.W. Strapp, 1993, pers. commun.). The pattern of background light recorded by the CDS is displayed in
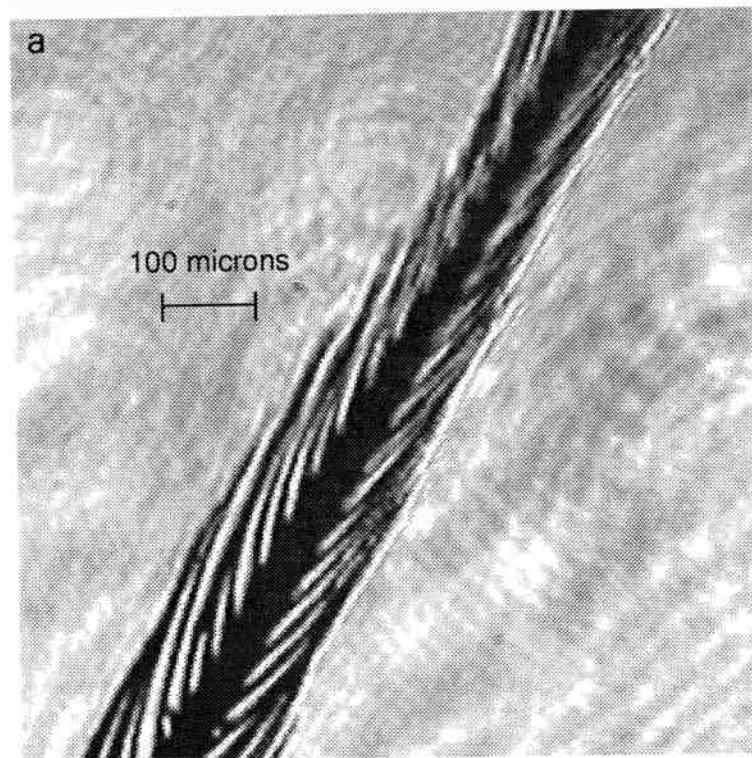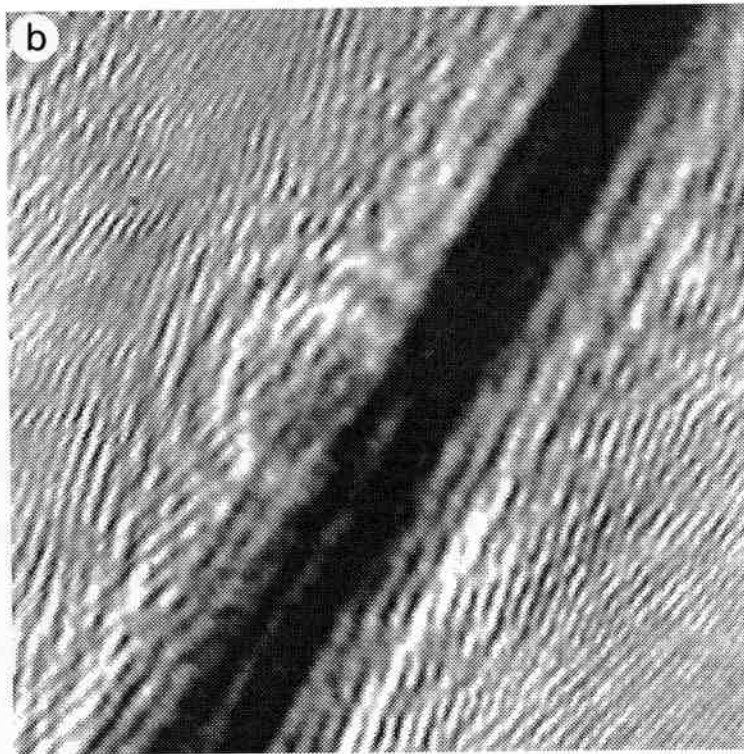
real-time, so that if there were any optical contamination it would be obvious as soon as the spray nozzles are turned off.

The standard used for LWC measurements in non-icing conditions in the NRC tunnel is the King LWC probe (King et al., 1978, 1985). A modified FSSP-100 with 15 size bins, each with 6 μm size resolution was used to determine size spectra; however, NRC personnel have found that integrating the drop spectra from this (modified) FSSP to give LWC usually produces errors when LWC > 1 g m^{-3}.

Nine different tunnel spray settings were used during a 40 min test. Fig. 14 shows FSSP and King LWC, FSSP drop concentration and tunnel speed during the test. The droplet spectra from the first eight runs were very similar and the drop concentration increased to produce proportional increases in LWC. The air pressure to the spray nozzles was decreased before setting 9 which shifted the spectrum toward larger sizes. Fig. 15 shows a comparison of the drop spectra for spray settings 8 and 9.

The individual optical weighing functions, normalized LWC output function and LWC for the SPEC instrument are shown in Fig. 16. Note that processing the angular measurements in software instead of using optical filters allows for the use of negative weighting functions, which produces a nearly flat output function out to drop diameters of 75 μm. (Theoretical computations suggest that for a
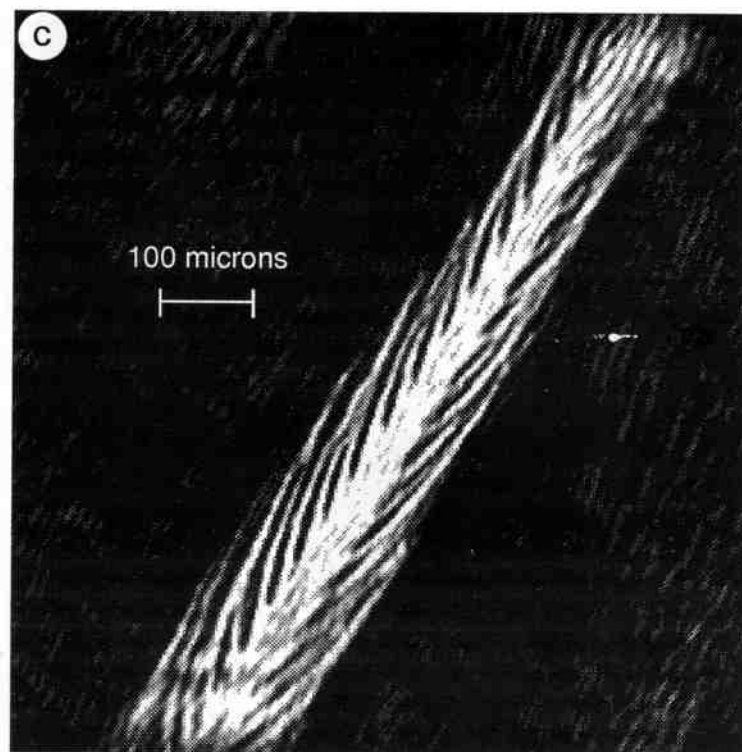
Fig. 10. In-focus image (a) of barb of feather from Guinea bird. Hologram of feather (b) was taken 0.5 cm from focal plane. Image shown in inverse video (c) was numerically reconstructed from hologram and demonstrates capability of DHIS to reproduce fine detail of features (barbules as small as $3 \mu m$).

CDS with these optics, a flat output function can be achieved out to about 150 μm.)

Fig 17 shows a comparison in LWC measurements from the King, FSSP and SPEC probes for the 9 spray settings used in the tunnel. Very good agreement is seen between the King and SPEC probes, and as expected, the FSSP LWC diverges from the King values at concentrations $> \sim 1$ g m^{-3}. Also, notice in Fig. 16 that the output of the CDS returns very accurately to zero each time the spray is off. This is an intrinsic characteristic of the instrument, i.e., it is not necessary to perform any calibration to achieve this.

3.3. Droplet spectrum measurement

Theory

For an ensemble of droplets, described by a size distribution function (size spectrum), $f(r)$, the total scattered intensity is
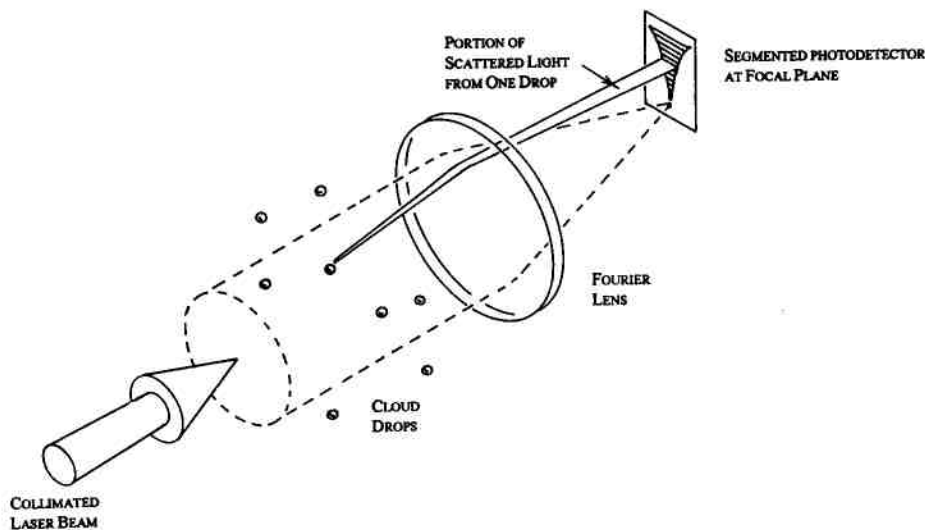
Fig. 11. Schematic drawing showing how light scattered from a drop at one particular angle is transformed into a unique signal on a segmented photodetector.

$$I(\theta) = \int_{r=0}^{\infty} K(\theta,r) * f(r) \, dr, \tag{5}$$

where $K(\theta,r)$ is the normalized droplet scattering function introduced in Eq. (4). This assumes that the scattered light pattern of an ensemble can be described as the linear superposition of the pattern from each droplet. This assumption is valid if two conditions hold:

(i) There is little multiple scattering. This assumption is valid to nearly 50% extinction of the incident beam (Blyth et al., 1984).

(ii) The scattered light adds incoherently. This is true if there are many droplets ($\geqslant 100$), so that interference effects average out.

Since $I(\theta)$ is measured and $K(\theta,r)$ can be calculated by diffraction theory for ideal, or Monte-Carlo methods for real optical systems; Eq. (5) can be inverted to yield $f(r)$, the droplet size spectrum.

An analytical solution for Eq. (5) was found (independently) by Chin et al. (1955) and by Shifrin (1956) for the droplet distribution, $f(r)$, for the specific case where the scattering function, $K(\theta,r)$, is approximated by means of diffraction theory. That is, if in Eq. (5) the scattering function, $K(\theta,r)$, is given by

$$K(\theta,r) = \frac{I(0) \, [2\pi r J_1(2\pi)]^2}{\theta^2}. \tag{6}$$

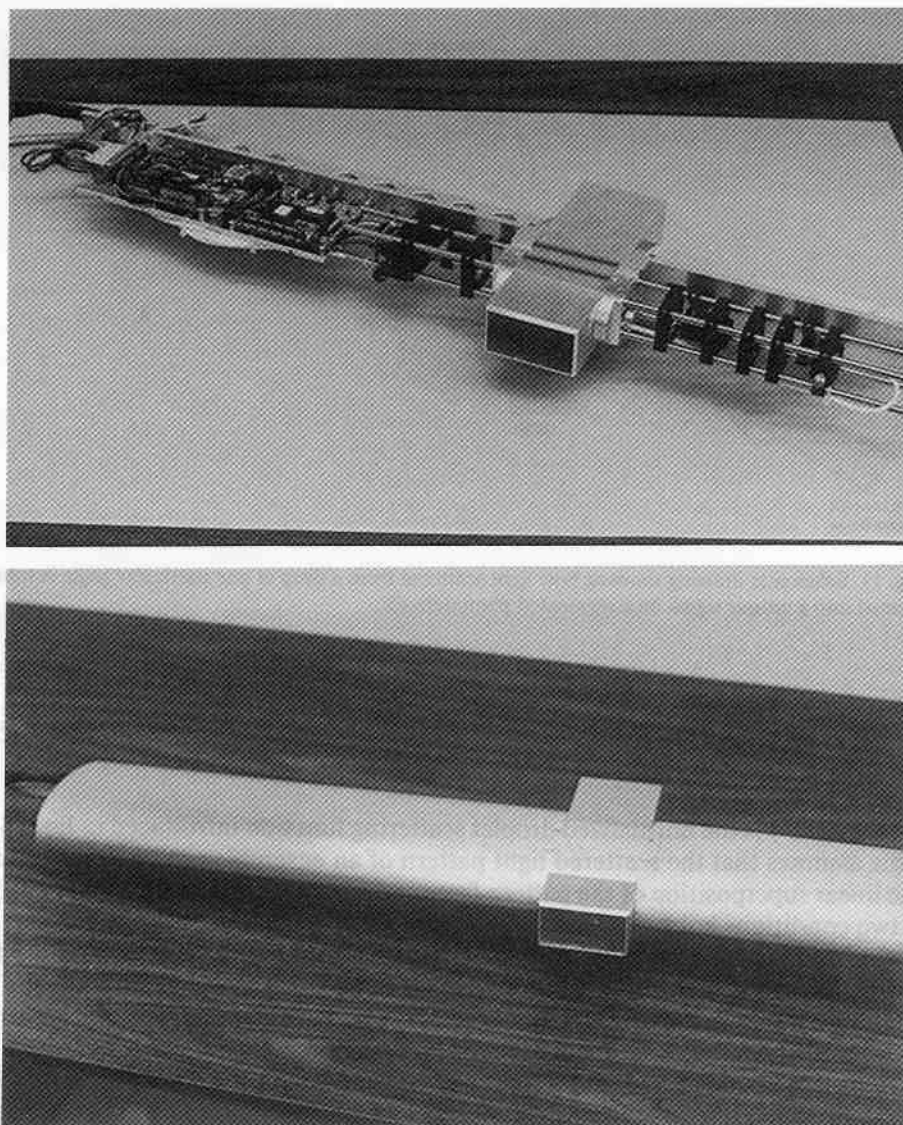Then, the droplet distribution, $f(r)$ is given by

Fig. 12. Photographs of (top) microbench optics and CCD electronics and (bottom) same components packaged in an airfoil strut for testing in the NRC icing wind tunnel. The laser beam enters and exits the sample volume (rectangular tube) via special non-wetting windows (see text for further discussion).

$$f(r) = -\frac{\pi^2}{r^2} \int\limits_0^\infty \chi(x\theta)\psi(\theta)\mathrm{d}\theta, \tag{7}$$
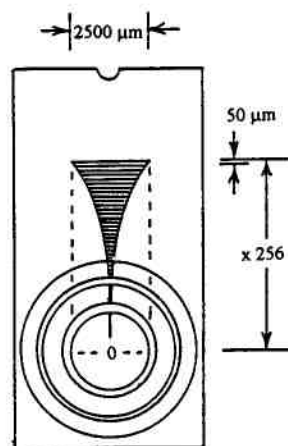
Fig. 13. Schematic diagram of CCD array with mask that enhances dynamic range. The 256 CCD pixels are 50 μm high by 2500 μm wide. The circles represent scattered light from a single droplet.

where

$$\chi(x\theta) \equiv x\theta J_1(x\theta) Y_1(x\theta); \quad x \equiv 2\pi r, \qquad \psi(\theta) \equiv \frac{d}{d\theta}\left(\theta^3 \frac{I(\theta)}{I(0)} \right) \tag{8}$$

and J_1, Y_1 are Bessel functions of the first and second kinds.

The analytical solution appears attractive, but is difficult to apply to optical systems that include non-ideal effects, such as vignetting, noisy and missing data. It is also somewhat ironic that the *analytical* solution actually requires more computer time to calculate (due to the Bessel functions) than *numerical* methods. However, the θ_3 term that appears in the analytical solution Eqs. (6)–(8) is a useful weighting function in numerical solutions and is the basis for the gain function used in the CDS; i.e., the V-shaped mask (Fig. 13) produces θ^2 and variable electronic gain achieves an additional factor of θ, resulting in an effective gain of θ^3.

Several candidate numerical solutions are discussed in Riley and Agrawal (1991). In general, numerical solutions can be posed in the following way: Assuming that we sample the scattered light at a number of discrete angles, θ_j, $j = 1 \to M$, and that we wish to know the droplet spectra, $f(r)$, at a range of discrete radii, r_i, $i = 1 \to N$, we can then approximate Eq. (8) with a summation:

$$I(\theta_j) = \sum_{i=1}^{N} K(\theta_j, r_i) * f(r_i), \quad (j = 1 \to M), \tag{9}$$

or, in matrix notation,

$$\vec{I} = K^t * \vec{f},$$

where the matrix, K^t, can be seen to be the transpose of the matrix in Eq. (4).

This system of equations can then be solved for the droplet spectra, $f(r)$, if the
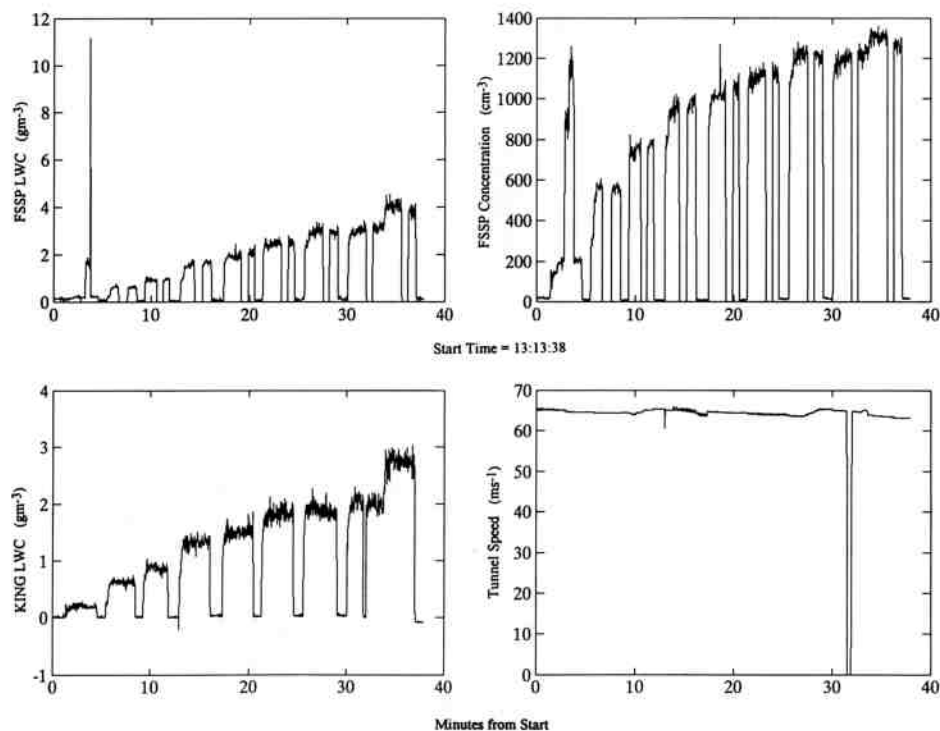
Fig. 14. Data from the NRC icing wind tunnel. Upper Left: Liquid Water Content (LWC) from the PMS FSSP probe Upper Right: Drop concentration from FSSP. Lower Left: King Probe Liquid Water Content.

system is well-enough conditioned. The conditioning of the equation system can be sensed and repaired by the analysis program itself. The numerical method used must successfully contend with two unavoidable problems; noisy data and missing data. In general, data can be missing from both large angles, (θ), due to the limited size of the photodetector array, and at small angles due to the geometry of the instrument or interference by the strong unscattered beam.

The methods available to deal with imperfect data are first, to adjust the ranges of θ_j and r_i in Eq. (9), and second in the choice of solution technique. The basic methods are as follows:

(i) Adjustment of variable range:

The range and spacing of angles over which data are taken is limited by the design of the instrument. In general, the larger the range and the finer the spacing of data in θ, the more information that can be recovered about the distribution $f(r)$. Numerical simulations by Cormack and Lawson (1993b) have shown that the number of bins, i in r_i for which information can be reliably recovered from a number of measurements, j, of $I(\theta_j)$ (assuming no more than 5% noise level) is approximately $i = j/4$. Thus, the linear sys-
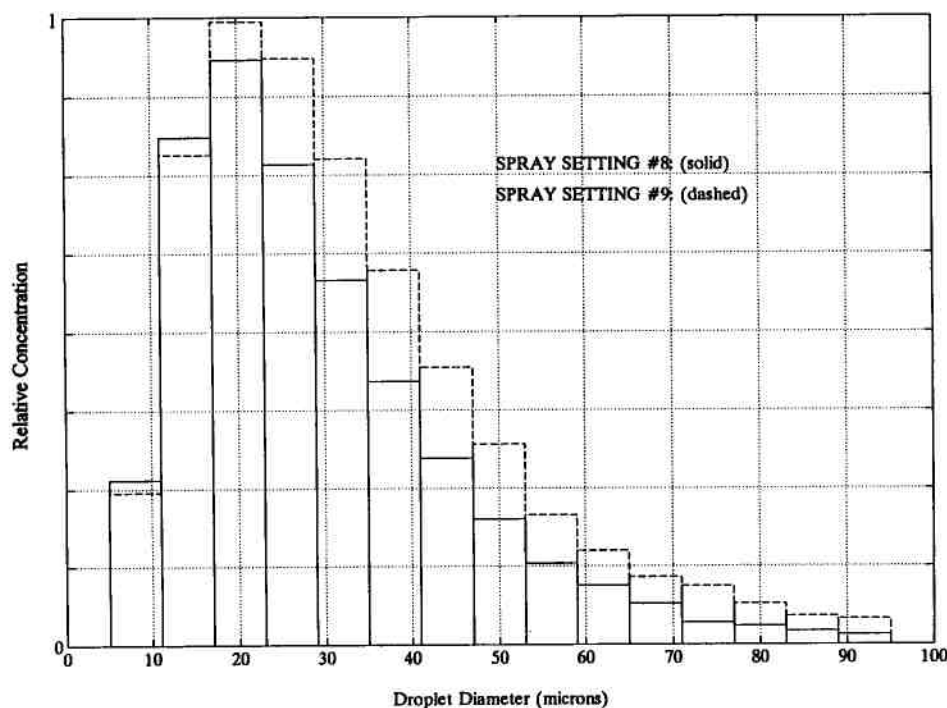
FSSP SPECTRA #8 & #9

Fig. 15. FSSP droplet spectra for spray settings 8 and 9 in the NRC wind tunnel.

tem, Eq. (9), must be overdetermined by a factor of four.

Missing data are accounted for by adjusting the ends of the size range, r_i. Data missing at the low angle end of θ_j are compensated by limiting r_i to below a maximum size. Data missing at the large angle end of θ_j are compensated by similarly limiting the range of r_i to be above a minimum size.

(ii) Solution techniques:

Numerical solution techniques fall roughly into two categories, unconstrained and constrained. The unconstrained technique is just the solution of the overdetermined system Eq. (9) by the means of least squares. Constrained techniques are the least squares method constrained to produce various results such as non-negative values for $f(r_i)$, or a "smooth" $f(r_i)$ (i.e., the "Phillips–Twomey" method—see Bayvel and Jones, 1981).

Constrained techniques usually require an iterative solution algorithm that must be repeated for each new data set, while the unconstrained technique can be encoded into a "pseudo-inverse" matrix, and each subsequent droplet distribution found requires only a matrix-vector multiply to generate.
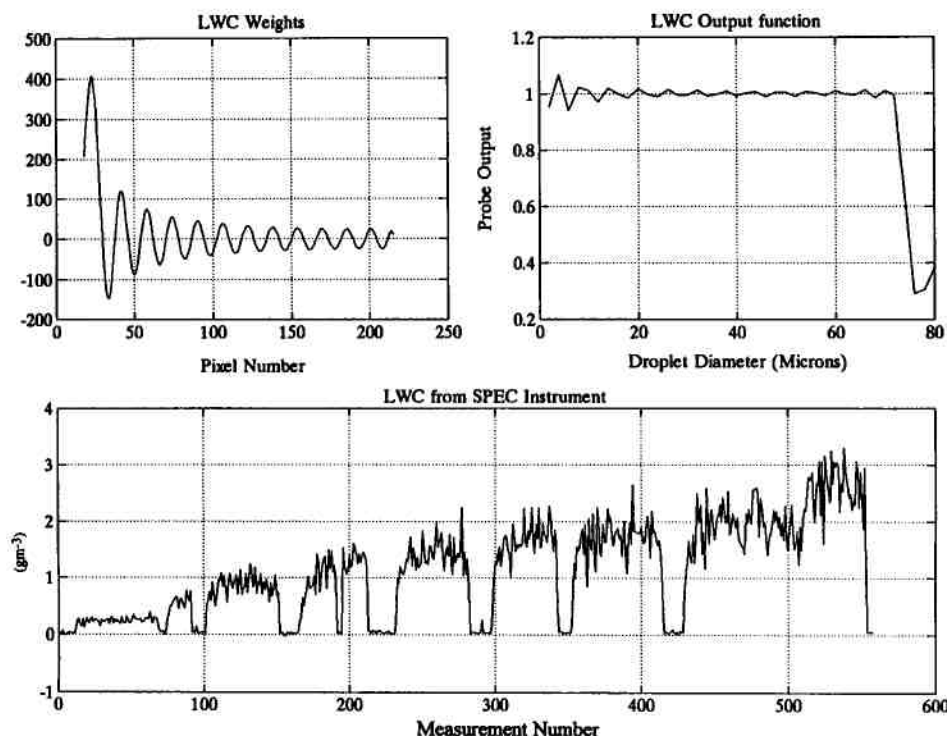
Fig. 16. Graphs of (upper left) pixel weighting function, (upper right) calculated output function and (bottom) resulting LWC output from the SPEC instrument during the NRC wind tunnel test. (Note: the SPEC instrument was sampled intermittently during the tests so that the horizontal axis on the bottom panel is not a continuous time scale.)

Measurements of drop spectra

Since precisely-sized drops are difficult to generate and suspend in the laboratory and there is no standard measurement device, we investigated the particle sizing capability of the CDS using aqueous suspensions of polystyrene spheres.[3]

Suspensions of spheres with known size distributions (obtained from Duke Scientific in Palo Alto, California) were placed in optical-quality spectrographic sample cells (supplied by NSG Precision Cells Inc. of Farmingdale, New York) and the cells placed in the sample area of the CDS.

A number of corrections to the numerical calculations and to the physical setup

---

[3] We did not compare the drop-size spectra measured by the FSSP and CDS during the Ottawa wind tunnel tests (discussed in the previous section). This was because the background light level in the first prototype version of the CDS was too high for good recovery of drop size spectra. The relatively high background light level was due to scattering of light from the mask which was bonded to the quartz coverplate about 1 mm in front of the CCD array. Improvements to the prototype were made by adding optics to relay the image of the V-shaped mask directly onto the CCD array, thus eliminating the stray light scattered from the mask.
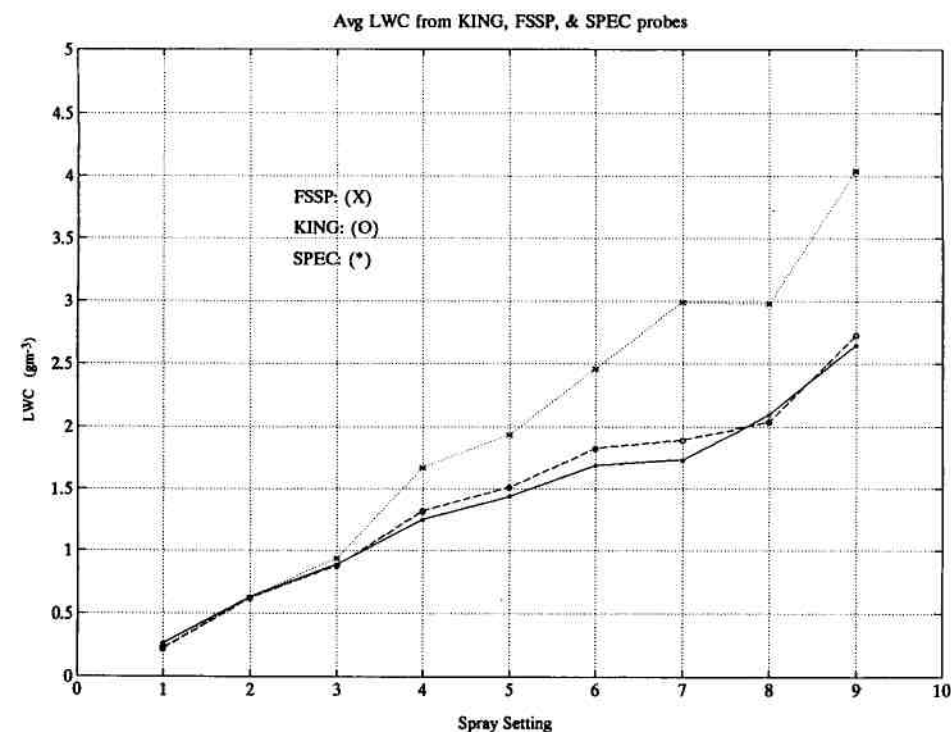
Avg LWC from KING, FSSP, & SPEC probes

Fig. 17. Comparison of LWC measurements during the NRC wind tunnel test from the FSSP (dotted line), King Probe (dashed line) and SPEC instrument (solid line).

were needed to correct for the differences between this test setup and the measurement of cloud droplets:

(i) The scattering functions were re-calculated (using Mie theory) accounting for the index of polystyrene spheres (1.579) in water (1.328) at a wavelength of 0.78 μm.

(ii) The change (increase) in scattering angle of the light leaving the water-filled test cell had to be accounted for, using the refraction relation

$$\sin(\theta_{air}) = \frac{n_{water}}{n_{air}} \sin(\theta_{water}). \tag{10}$$

(The effect of the intermediate glass interface cancels out.)

(iii) In order to prevent interference fringes due to multiple reflections in the test cell from contaminating the data, the test cells had to be rotated $\approx 15°$ from the normal incidence angle to the beam.

With these modifications to the numerical and physical setup, we were able to obtain *excellent* agreement between (Mie) theory and CDS measurements of light scattered from suspensions of polystyrene spheres in the laboratory. For example, Fig. 18 shows plots of the (top) measured and (bottom) theoretical intensity of
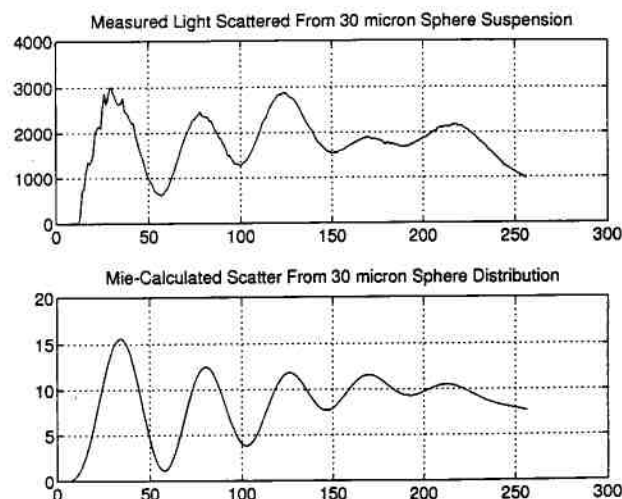
Measured Light Scattered From 30 micron Sphere Suspension

Mie-Calculated Scatter From 30 micron Sphere Distribution

Fig. 18. Comparison of (top) light scattered from an aqueous suspension of polystyrene spheres with 30 μm diameters, as measured by the Cloud Drop Spectrometer (CDS) in the laboratory, and (bottom) theoretical prediction of light scattered from 30 μm polystyrene spheres using Mie theory. (The vertical scale of the theoretical plot has been multiplied by the effective gain used in the CDS.)

scattered light from a suspension of 30 μm polystyrene spheres.[4] The x-axis is in pixel number and the y-axis is in digitizer counts. The background reading has been subtracted from the data. The bottom plot in Fig. 18 shows the expected signal calculated from Mie theory (y-axis is arbitrary). To calculate these data, we have included compensation for the (θ^3) instrument gain (due to the variable size mask, variable integration time, and optics vignetting), plus the finite width of the size distribution and its Gaussian shape. It is worthwhile noting that, in order to produce an output such as Fig. 18, the prototype CDS is measuring light intensities that vary by nearly six orders of magnitude over a distance of only 1 cm on the CCD array.

The jagged sub-peaks on the top curve in Fig. 18 are due to speckle noise, and limit the size of the largest drops measurable. When the period of the scattered light is small enough (for large drops) then the signal cannot be separated from the speckle noise by low-pass filtering. At this point, results become unreliable. The exact size where this happens has yet to be precisely determined and depends to some extent on the technique of signal recovery, but we estimate it to be ~150 μm drop diameter.

Although results from the measurements and theory are very similar, (i.e., Fig. 18) there are still some discernible differences, especially at the low and high angle ends of the data. Some of this difference is due to inaccuracies in the cal-

---

[4] The manufacturer quotes a mean size and standard deviation of 29.9 μm ± 0.2 μm for the 30 μm solution of spheres. The other solutions tested were not as precise, having means and standard deviations of 3.4 μm ± 0.8 μm, 10.2 μm ± 1.9 μm and 21.7 μm ± 3.2 μm.
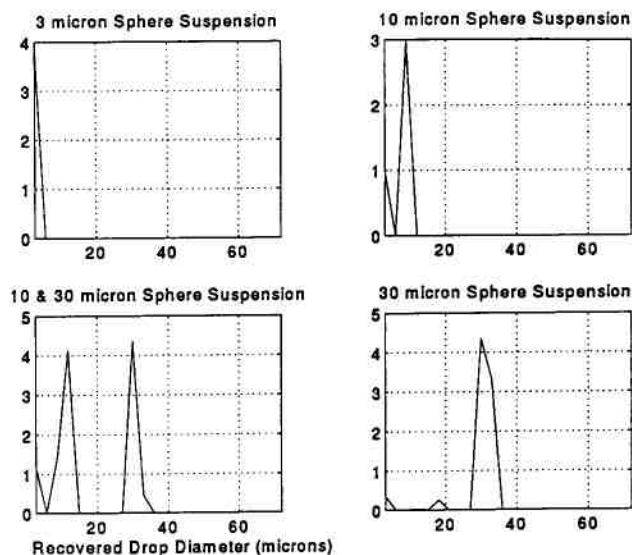
Fig. 19. Size spectra recovered from laboratory measurements through test cells filled with aqueous suspensions of polystyrene spheres (see text for further discussion).

culation of the instrument gain curve (gain vs. scattering angle). This can be corrected with more laboratory calibrations. Another difference factor is the non-ideal features of the test sample. Microscopic examination of the polystyrene sphere sample shows a small percentage of broken spheres and clustered spheres. The light scattering contribution of these defects cannot be calculated, and is therefore not known.

Using the modified Phillips–Twomey numerical method mentioned previously, we were able to extract the size spectrum and concentration of polystyrene spheres for sizes from 3.4 μm to 30 μm, as shown in Fig. 19. These figures show good recovery of mono-dispersed and bimodal size distributions of the polystyrene spheres. The small spread in the (mono-dispersed) distributions may be due to many factors, including break-up and clustering of the spheres, changes in the index of refraction of the medium due to changes in temperature, uncertainty in the gain function of the CDS and limitations of the numerics. In atmospheric applications, problems with clustering and variation of index of refraction in the medium will not be present. Quantification of the gain function can be improved through more sophisticated laboratory measurements and with more study the numerics can be refined.

4. Summary

Measurement limitations of current cloud microphysical instrumentation produce significant uncertainties in drop-size spectra, liquid water content (LWC)

and the concentration and shape of small ice crystals. Two new instruments with potential to reduce these measurement uncertainties were described theoretically and results of laboratory and wind tunnel tests were discussed.

A Digital Holographic Imaging System (DHIS) uses digital in-line holography to extend the optical depth-of-field (*DOF*) over in-focus imaging techniques by up to a factor of 1000. Extending the *DOF* provides a commensurate increase in sample volume, a limiting factor in conventional optical imaging systems. Laboratory tests of the Signal/Noise (S/N) of the DHIS showed a 10–20 times improvement over optical (film) holography. This improvement facilitates (for the first time with high confidence) automated analysis of the size and three-dimensional positioning of cloud drops. Besides providing three-dimensional drop spacing, this also gives an explicit measurement of LWC. Additional laboratory tests suggest that the improved S/N has also made possible a significant reduction in the minimum detectable drop size, from about 6 μm to ~ 2 μm. The DHIS can also give high-resolution measurements of the size and shape of small ice crystals. This information is needed to determine the optical scattering properties of cirrus clouds and the origin of small ice in water clouds.

The second instrument described, a Cloud Drop Spectrometer (CDS), measures with high (0.035°) angular resolution the forward scattered light from an ensemble of cloud drops. A CCD array with 256 photodiodes measures the scattered light. The inherent limitations associated with single-drop scattering measurements (i.e., small sample volume and coincidence errors) are eliminated. LWC is computed by weighting the angular measurements in software using a technique reported in Blyth et al. (1984). The ability to perform the calculations in software allows for negative weights, which is not possible when the weighting is done optically. Also, measurements of raw scattered light can be used to remove changes in background illumination, providing an autocalibration feature. CDS measurements of LWC in an icing wind tunnel agreed well with the tunnel standard. Drop-size spectra are computed in software using inversion techniques. Laboratory measurements of aqueous solutions of polystyrene spheres strongly suggest that the CDS can accurately size drops in water clouds; however, more laboratory and controlled wind tunnel tests are needed.

Acknowledgments

References

Bachalo, W.D. and Houser, M.J., 1984. Phase/Doppler spray analyzer for simultaneous measurements of drop size and velocity distributions. Opt. Eng., 23: 583–590.

Baker, M.B., Breidenthal, R.E., Choularton, T.W. and Latham, J., 1984. The effects of turbulent mixing in clouds. J. Atmos. Sci., 41: 299–304.

Baker, B.A., 1992. Turbulent entrainment and mixing in clouds: A new observational approach. J. Atmos. Sci., 49: 387–404.

Baumgardner, D., 1983. An analysis and comparison of five water droplet measuring instruments. J. Appl. Meteorol., 22: 891–910.

Baumgardner, D., Strapp, W. and Dye J.E., 1985. Evaluation of the forward scattering spectrometer probe. Part II: Corrections for coincidence and dead-time losses. J. Atmos. Oceanic Technol., 2: 626–632.

Bayvel, L.P. and Jones, A.R., 1981. Electromagnetic Scattering and its Applications. Applied Science, New Jersey.

Beard, K.V. and Ochs, H.T., III, 1993. Warm-rain initiation: An overview of microphysical mechanisms. J. Appl. Meteorol., 22: 608–625.

Bexon, R., Gibbs, J. and Bishop, J.D., 1976. Automatic assessment of aerosol holograms. J. Aerosol Sci., 7: 397–407.

Biter, C.J., Dye, J.E., Huffman, D. and King, W.D., 1987. The drop-size response of the CSIRO liquid water content probe. J. Atmos. Oceanic Technol., 4: 359–367.

Blyth, A.M., 1993. Entrainment in cumulus clouds. J. Atmos. Oceanic Technol., 4: 626–641.

Blyth, A.M., Chittenden, A.M.I. and Latham, J., 1984. An optical device for the measurement of liquid water content in clouds. Q. J. R. Meteorol. Soc., 110: 53–63.

Borrmann, S. and Jaenicke, R., 1993. Application of microholography for ground-based in situ measurements in stratus cloud layers: A case study. J. Atmos. Oceanic Technol., 10: 277–293.

Born, M. and Wolf, E., 1965. Principles of Optics. Third Ed., Pergamon Press, Oxford, 808 pp.

Brenguier, J.L., 1989. Coincidence and dead-time corrections for particle counters. Part II: High concentration measurements with an FSSP. J. Atmos. Oceanic Technol., 6: 585–598.

Brenguier, J.L., Rodi, A.R., Gordon, G. and Weschler, P., 1993. Realtime detection of the performance degradation of the Forward Scattering Spectrometer Probe. J. Atmos. Oceanic Technol., 10: 27–33.

Brown, P.R.A., 1989. Use of holography for airborne cloud physics experiments. J. Atmos. Oceanic Technol., 6: 293–306.

Chin, J.H., Sliepcevich, C.M. and Tribus, M., 1955. Particle size distributions from angular variation of forward-scattered light at very small angles. J. Phys. Chem., 59: 841–844.

Chittenden, A.M.I., 1976. The Determination of Cloud Droplet Size Distributions by Light Scattering. Ph.D. Diss., Univ. Manchester, England.

Cooper, W.A., 1988. Effects of coincidence on a forward scattering spectrometer probe. J. Oceanic Atmos. Tech., 5: 823–832.

Cooper, W.A. and Vali, G., 1981. The origin of ice in mountain cap clouds. J. Atmos. Sci., 38: 1244–1259.

Cooper, W.A.and Lawson, R.P., 1984. Physical interpretation of results from the HIPLEX-1 Experiment. J. Appl. Meteorol, 23: 523–540.

Cormack, R.H. and Lawson, R.P., 1993a. A digital holographic technique for automatic analysis of particle fields. Appl. Opt. (in progress)

Cormack, R.H. and Lawson, R.P., 1993b. Sizing of spherical particles using automated measurements of far-field diffraction from a field of drops. Appl. Opt. (in progress)

Dowling, D.R. and Radke, L.F., 1990. A summary of the physical properties of Cirrus clouds. J. Appl. Meteorol., 29: 970–978.

Dye, J.E., Knight, C.A., Tootenhoofd, V. and Cannon, T.W., 1974. The mechanism of precipitation formation in northeastern Colorado cumulus. III. Coordinated microphysical and radar observations and summary. J. Atmos. Sci., 31: 2152–2159.

Gabor, D., 1949. Microscopy by reconstructed wave-fronts. Proc. R. Soc., A197: 454–487.

Gerber, H., 1992. New microphysics sensor for aircraft use. Preprints: 11th ICCP Int. Conf. Clouds and Precipitation, Montreal, pp. 942–945.

Grabowski, W., 1983. Measurement of the size and position of aerosol droplets using holography. Optics Laser Tech., 14: 199–205.

Heymsfield, A.J. and Baumgardner, D., 1985. Summary of a workshop on processing 2D probe data. Bull. Am. Meteorol. Soc., 66: 437–440.

Heymsfield, A.J., Miller, K.M. and Spinhirne, J.D., 1990. The October 27–28 1986, FIRE case study: Cloud microstructure. Mon. Weather Rev., 118: 2313–2328.

Hirleman, E.D., Oechsle, V. and Chigier, N.A., 1984. Response characteristics of laser diffraction particle size analyzers: optical sample volume extent and lens effects. Opt. Eng., 23: 610–619.

King, W.D., Parkin, D.A. and Handsworth, R.J., 1978. A hot-wire water device having fully calculable response characteristics. J. Appl. Meteorol., 17: 1809–1813.

King, W.D., Dye, J.E., Strapp, J.W., Baumgardner, D. and Huffman, D., 1985. Icing wind tunnel tests on the CSIRO liquid water content probe. J. Atmos. Oceanic Technol., 2: 340–352.

Knollenberg, R.G., 1970. The optical array: An alternative to scattering or extinction for airborne particle size determination. J. Appl. Meteorol., 9: 86–103.

Knollenberg, R.G., 1981. Techniques for probing cloud microstructure. In: P.V. Hobbs and A. Deepak (Editors), Clouds, Their Formation Optical Properties and Effects. Academic Press, New York, pp. 15–92.

Korolev, A.V., Kuznetsov, S.V., Makarov, Y.E. and Novikov, V.S., 1991. Evaluation of measurements of particle size and sample area from optical array probes. J. Atmos. Oceanic Technol., 8: 514–522.

Kozikowsha, A., Haman, K. and Supronowicz, J., 1984. Preliminary results of an investigation of the spatial distribution of fog droplets by a holographic method. Q. J. R. Meteorol. Soc., 110: 65–73.

Lawson, R.P.F and A.R. Rodi, 1992. A new airborne thermometer for atmospheric and cloud physics research. Part I. Design and preliminary flight tests. J. Atmos. Oceanic Technol., 9: 556–574.

Lawson, R.P., R.E. Stewart, J.W. Strapp and G.A. Isaac, 1993. Airborne measurements of the origin and growth of very large snowflakes. Geophys. Res. Lett., 20: 53–56.

Oldenburg, J.R. and Ide, R.F., 1990. Comparison of Two Droplet Sizing Systems in an Icing Wind Tunnel. NASA TM-102456, (AIAA-90-0668), NASA Lewis Research Center, 20 pp.

Pruppacher, H.R., and Klett, J.D., 1978. Microphysics of clouds and precipitation. Reidel, Boston. 714 pp.

Riley, J.B. and Agrawal, Y.C., 1991. Sampling and inversion of data in diffraction particle sizing. Appl. Opt., 30: 4800–4817.

Shifrin, K.S., 1956. Tr. VSLTI (Leningrad), 2: 153–162.

Strapp, J.W., and Schemenauer, R.S., 1982. Calibrations of Johnson–Williams liquid water meters in a high-speed icing tunnel. J. Appl. Meteorol., 21: 98–108.

Swithenbank, J., Beer, J., Taylor, D.S., Abbot, D. and McCreath, C.G., 1977. In: B.T. Zinn (Editor), Experimental Diagnostics in Gas-Phase Combustion Systems. AIAA Progress in Astronautics and Aeronautics. A laser diagnostic technique for the measurement of droplet and particle size distribution. AIAA, 53: 421–427.

Trolinger, J.D., 1985. Particle and flow field holography. A critical survey. SPIE J., 532: 40–61.

Wielicki, B.A., Suttles, J.T., Heymsfield, A.J., Welch, R.M., Spinhirne, J.D., Wu, Man-Li C., Starr, D.O'C., Parker, L. and Arduini, R.F., 1990. The 27–28 October 1986 FIRE IFO cirrus case study: Comparison of radiative transfer theory with observations by satellite and aircraft. Mon. Weather Rev., 118: 2356–2376.

Zarschitzky, H., 1985. Digitale Hologrammauswertung von Pulsholografisch Aufgezeichneten Blasenfeldern (Digital analyses of bubble fields recoreded with pulsed holography). Diss., Universität Goettingen.